



Short GRB 160821B: A Reverse Shock, a Refreshed Shock, and a Well-sampled Kilonova

G. P. Lamb¹, N. R. Tanvir¹, A. J. Levan^{2,3}, A. de Ugarte Postigo^{4,5}, K. Kawaguchi^{6,7}, A. Corsi⁸, P. A. Evans¹, B. Gompertz², D. B. Malesani^{5,9}, K. L. Page¹, K. Wiersema^{1,2}, S. Rosswog¹⁰, M. Shibata^{7,11}, M. Tanaka¹², A. J. van der Horst^{13,14}, Z. Cano¹⁵, J. P. U. Fynbo⁹, A. S. Fruchter¹⁶, J. Greiner¹⁷, K. E. Heintz¹⁸, A. Higgins¹, J. Hjorth⁵, L. Izzo⁴, P. Jakobsson¹⁸, D. A. Kann⁴, P. T. O’Brien¹, D. A. Perley¹⁹, E. Pian²⁰, G. Pugliese²¹, R. L. C. Starling¹, C. C. Thöne⁴, D. Watson⁹, R. A. M. J. Wijers²¹, and D. Xu²²

¹ University of Leicester, Department of Physics & Astronomy and Leicester Institute of Space & Earth Observation, University Road, Leicester, LE1 7RH, UK
gpl6@leicester.ac.uk

² Department of Physics, University of Warwick, Coventry, CV4 7AL, UK

³ Department of Astrophysics, Radboud University, 6525 AJ Nijmegen, The Netherlands

⁴ Instituto de Astrofísica de Andalucía (IAA-CSIC), Glorieta de la Astronomía s/n, E-18008 Granada, Spain

⁵ DARK, Niels Bohr Institute, University of Copenhagen, Lyngbyvej 2, DK-2100 Copenhagen Ø, Denmark

⁶ Institute for Cosmic Ray Research, The University of Tokyo, 5-1-5 Kashiwanoha, Kashiwa, Chiba 277-8582, Japan

⁷ Center for Gravitational Physics, Yukawa Institute for Theoretical physics, Kyoto University, Kyoto 606-8502, Japan

⁸ Department of Physics and Astronomy, Texas Tech University, Lubbock, TX 79409, USA

⁹ The Cosmic DAWN Center, Niels Bohr Institute, University of Copenhagen, Lyngbyvej 2, DK-2100 Copenhagen Ø, Denmark

¹⁰ The Oskar Klein Centre, Department of Astronomy, AlbaNova, Stockholm University, SE-106 91 Stockholm, Sweden

¹¹ Max Planck Institute for Gravitational Physics (Albert Einstein Institute), Am Mühlenberg 1, Potsdam-Golm, D-14476, Germany

¹² Astronomical Institute, Tohoku University, Aoba, Sendai 980-8578, Japan

¹³ Department of Physics, The George Washington University, 725 21st Street NW, Washington, DC 20052, USA

¹⁴ Astronomy, Physics, and Statistics Institute of Sciences (APStIS), 725 21st Street NW, Washington, DC 20052, USA

¹⁵ Berkshire College of Agriculture, Hall Place, Burchett’s Green Road, Burchett’s Green, Maidenhead, UK

¹⁶ Space Telescope Science Institute, 3700 San Martin Drive, Baltimore, MD 21218, USA

¹⁷ Max-Planck Institut für extraterrestrische Physik, D-85748 Garching, Giessenbachstr. 1, Germany

¹⁸ Centre for Astrophysics and Cosmology, Science Institute, University of Iceland, Dunhagi 5, 107 Reykjavík, Iceland

¹⁹ Astrophysics Research Institute, Liverpool John Moores University, IC2, Liverpool Science Park, 146 Brownlow Hill, Liverpool L3 5RF, UK

²⁰ INAF, Astrophysics and Space Science Observatory, via P. Gobetti 101, I-40129 Bologna, Italy

²¹ Astronomical Institute Anton Pannekoek, University of Amsterdam, PO Box 94249, 1090 GE Amsterdam, The Netherlands

²² CAS Key Laboratory of Space Astronomy and Technology, National Astronomical Observatories, Chinese Academy of Sciences, Beijing 100012, People’s Republic of China

Received 2019 May 6; revised 2019 July 22; accepted 2019 August 4; published 2019 September 19

Abstract

We report our identification of the optical afterglow and host galaxy of the short-duration gamma-ray burst sGRB 160821B. The spectroscopic redshift of the host is $z = 0.162$, making it one of the lowest redshift short-duration gamma-ray bursts (sGRBs) identified by *Swift*. Our intensive follow-up campaign using a range of ground-based facilities as well as *Hubble Space Telescope*, *XMM-Newton*, and *Swift*, shows evidence for a late-time excess of optical and near-infrared emission in addition to a complex afterglow. The afterglow light curve at X-ray frequencies reveals a narrow jet, $\theta_j \sim 1.9_{-0.03}^{+0.10}$ deg, that is refreshed at >1 day post-burst by a slower outflow with significantly more energy than the initial outflow that produced the main GRB. Observations of the 5 GHz radio afterglow shows a reverse shock into a mildly magnetized shell. The optical and near-infrared excess is fainter than AT2017gfo associated with GW170817, and is well explained by a kilonova with dynamic ejecta mass $M_{\text{dyn}} = (1.0 \pm 0.6) \times 10^{-3} M_{\odot}$ and a secular (post-merger) ejecta mass with $M_{\text{pm}} = (1.0 \pm 0.6) \times 10^{-2} M_{\odot}$, consistent with a binary neutron star merger resulting in a short-lived massive neutron star. This optical and near-infrared data set provides the best-sampled kilonova light curve without a gravitational wave trigger to date.

Key words: gamma-ray burst: individual (GRB 160821B) – stars: neutron

1. Introduction

Short-duration gamma-ray bursts (sGRBs) are widely thought to result from the merger of a binary neutron star (BNS) or a neutron star and a stellar mass black hole system. A fraction of the neutron star matter disrupted during the inspiral or collision will undergo rapid accretion onto the remnant object and launch an ultra-relativistic jet (e.g., Nakar 2007; Gehrels et al. 2009). Energy dissipation within such a jet produces a GRB, and, as this outflow decelerates, an external shock forms producing broadband afterglow emission. This progenitor model is supported by the fact that well-localized sGRBs (mainly the sample discovered by the *Neil Gehrels Swift Observatory*, hereafter referred to as *Swift*) appear to be produced in a wide range of stellar populations, including those

with no recent star formation, and on occasions at large distances (tens of kiloparsecs in projection) from their putative host galaxies (e.g., Fong et al. 2013; Tunnicliffe et al. 2014).

A further signature of compact binary mergers involving neutron stars is via the observation of a slower transient, variously called a “macronova” (Kulkarni 2005), “kilonova” (Metzger et al. 2010), or “merger-nova” (Gao et al. 2015; in this paper we shall use the term kilonova). A kilonova is powered by the radioactive decay of heavy, unstable, neutron-rich species created from decompressed neutron star material, which is ejected during the merger (e.g., Li & Paczyński 1998).

The first compelling observational evidence for such a kilonova was the case of sGRB 130603B, for which excess near-infrared emission was detected in *Hubble Space Telescope* (*HST*) imaging at about one week in the rest frame after the

event (Berger et al. 2013; Tanvir et al. 2013). That this excess appeared in the near-IR tallied with predictions that the same heavy r-process elements created in the kilonova should produce dense line-blanketing in the optical, leading to emission appearing in the near-IR in the days to weeks following the merger (Barnes & Kasen 2013; Kasen et al. 2013; Tanaka & Hotokezaka 2013). Further interest in these events comes from the fact that this process of radioactive decay naturally leads to stable r-process elements, thus potentially explaining the abundances of more than half the elements in the universe heavier than iron (e.g., Lattimer & Schramm 1974; Freiburghaus et al. 1999; Rosswog et al. 2018). Mapping the diversity and evolution of kilonova events over cosmic time is therefore an essential ingredient to quantifying their global contribution to nucleosynthesis.

At a redshift of $z = 0.36$ (de Ugarte Postigo et al. 2014), identifying the kilonova emission in the afterglow to sGRBs 130603B was challenging and would not currently be feasible at higher redshifts, where the bulk of well-localized sGRBs have been found. Indeed, state-of-the-art modeling of neutron star binary mergers suggests that ejection of sufficient material to create a kilonova as bright as this is unlikely to happen in most mergers, and may require special circumstances such as a high mass ratio for the components of the binary (e.g., Hotokezaka et al. 2013; Just et al. 2015; Sekiguchi et al. 2016). Nonetheless, following this discovery, and based on archival data, possible kilonova signatures were identified via a late-time I -band excess emission in two earlier GRBs; namely, sGRB 050709 at $z = 0.16$ (Jin et al. 2016) and GRB 060614 at $z = 0.125$ (Yang et al. 2015). More recently, it has been proposed that the optical counterparts identified for sGRB 070809 at $z = 0.22$ (Jin et al. 2019, although note that the host identification, and therefore redshift, in this case is rather uncertain) and sGRB 150101B at $z = 0.13$ (Troja et al. 2018) may have been dominated by kilonova emission. For GRB 060614 the claim is particularly controversial in that its prompt duration, $T_{90} \sim 100$ s, is much longer than the canonical $T_{90} \leq 2$ s for a sGRB. However, the absence of an accompanying bright supernova combined with it exhibiting an initial spike of gamma-rays with durations of only a few seconds has led to speculation that it could have been produced by a compact binary merger (Gal-Yam et al. 2006; Gehrels et al. 2006; Perley et al. 2009; Kann et al. 2011).

The recent multimessenger observation of the BNS merger GW170817, discovered via gravitational waves and associated with a burst of γ -rays, GRB 170817A, detected by *Fermi* and *INTEGRAL* (Abbott et al. 2017a, 2017b; Goldstein et al. 2017; Savchenko et al. 2017), provided an opportunity to test directly the merger progenitor model. GRB 170817A appeared faint when compared to the cosmological sample of sGRBs and by considering the compactness problem and lack of an early afterglow indicates that the burst of γ -rays is unlikely to be a typical sGRB seen off-axis (e.g., Lamb & Kobayashi 2018; Ziaepour 2018; Matsumoto et al. 2019); however, Ioka & Nakamura (2019) show that the observed GRB emission likely originates from a “mid”-region of a structured outflow. The rapid decline and superluminal motion of the late-time afterglow to GW170817 offer strong support for the sGRB–BNS association (Mooley et al. 2018; van Eerten et al. 2018; Ghirlanda et al. 2019; Lamb et al. 2019). Additionally, a kilonova was seen to follow GW170817, and monitored

intensively at UV, optical, and near-infrared wavelengths (e.g., Andreoni et al. 2017; Coulter et al. 2017; Cowperthwaite et al. 2017; Drout et al. 2017; Evans et al. 2017; Kasliwal et al. 2017b; Pian et al. 2017; Smartt et al. 2017; Tanvir et al. 2017; Utsumi et al. 2017). By scaling the well-sampled GW170817 kilonova light curve to the distance of sGRBs with afterglows, attempts have been made to investigate the diversity of the kilonova population (Ascenzi et al. 2019; Gompertz et al. 2018; Rossi et al. 2019).

Here we report a search with *HST*, *XMM-Newton*, and ground-based telescopes including the Gran Telescopio Canarias (GTC), the Nordic Optical Telescope (NOT), the Telescopio Nazionale Galileo (TNG), the William Herschel Telescope (WHT), and the Karl G. Jansky Very Large Array (VLA) for afterglow and kilonova emission accompanying sGRB 160821B, associated with a morphologically disturbed host galaxy at $z = 0.162$. We supplement these data with publicly available and/or published in other sources *Swift*, VLA, and *Keck* data. Throughout we assume a flat universe with $\Omega_m = 0.308$ and $H_0 = 67.8 \text{ km s}^{-1} \text{ Mpc}^{-1}$ (Planck Collaboration et al. 2016). Optical and near-IR magnitudes are reported on the AB system. In Section 2 we report the observations at X-ray, optical, near-IR, and radio frequencies plus the identification of the afterglow and the host. The results, interpretation, and afterglow and kilonova modeling are shown in Section 3. We discuss these results in Section 4 and give concluding remarks in Section 5.

2. Observations

2.1. Discovery of sGRB 160821B

The Burst Alert Telescope (BAT) on board *Swift* triggered on sGRB 160821B on 2016 August 21 at 22:29 UT. The reported duration of the burst was $T_{90}(15\text{--}350 \text{ keV}) = 0.48 \pm 0.07$ s (Palmer et al. 2016). The burst was also detected by *Fermi*/GBM, from which a somewhat longer duration of ≈ 1 s was found (Stanbro & Meegan 2016). Lü et al. (2017) performed a joint fit to the *Swift*/BAT and *Fermi*/GBM data, finding the total fluence in the 8–10,000 keV band of $(2.52 \pm 0.19) \times 10^{-6} \text{ erg cm}^{-2}$. This corresponds to an isotropic energy, assuming the redshift of $z = 0.162$, of $E_{\gamma, \text{iso}} = (2.1 \pm 0.2) \times 10^{50} \text{ erg}$, fairly typical of the population of short GRBs with measured redshifts (Berger 2014).

2.2. Afterglow Identification

After slewing, the X-ray Telescope (XRT) on *Swift* detected a fading afterglow that provided a refined localization, and from the X-ray spectrum found no evidence for significant absorption beyond that expected due to foreground gas in our Galaxy (Sbarufatti et al. 2016). As described below, our early optical imaging identified the afterglow of the burst and a prominent nearby galaxy at a separation of about $5''.7$ (Xu et al. 2016).

With a magnitude of $r \approx 19.4$ (Section 2.3), the probability of the chance alignment of an unrelated galaxy of this brightness or brighter this close to the line of sight is $P_{\text{chance}} \approx 1.5\%$ (using the formalism of Bloom et al. 2002) and although low, is not entirely negligible. However, the absence of any faint underlying quiescent emission in our final *HST* epochs (see Section 2.2), which might otherwise suggest a higher redshift host, adds support to our working hypothesis that this is the host galaxy of sGRB 160821B.

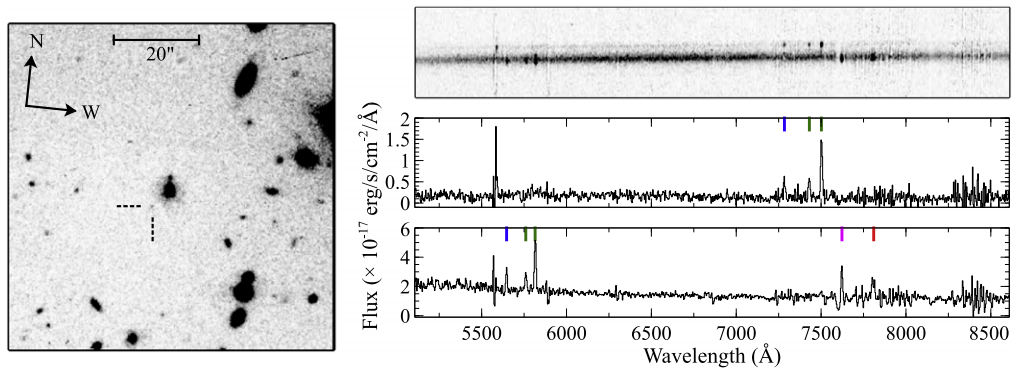


Figure 1. Left: WHT ACAM z -band image from 1.08 days post-burst, see Table 1. The transient location is indicated by the dashed lines. Right panels: the spectrum obtained with WHT/ACAM of the putative host galaxy at $z = 0.1616$ (brighter, lower trace showing prominent lines of $H\alpha$, $H\beta$, [S II], and [O III] indicated with short vertical lines in blue, pink, red, and green respectively) and a presumably unrelated background galaxy at $z = 0.4985$ (fainter, upper trace).

The NOT, located in the Canary Islands (Spain), began optical observations at 23:02 UT, only 33 minutes post-burst. These revealed an uncatalogued point source within the X-ray error region, presumed to be the optical afterglow (Xu et al. 2016). The best astrometry came from our *HST* images, and gave a position of R.A.(J2000) = 18:39:54.550, decl.(J2000) = +62:23:30.35 with an uncertainty of $\approx 0''.03$ in each coordinate, registered on the *GAIA* DR2 astrometric reference frame (Gaia Collaboration et al. 2016, 2018). Fong et al. (2016) reported a detection of the radio afterglow at 5 GHz with the VLA, which provided a burst location of R.A.(J2000) = 18:39:54.56, decl.(J2000) = +62:23:30.3 (reported error $0''.3$), consistent with our *HST* localization.

2.3. Host Galaxy and Redshift

The position of the proposed host galaxy measured from our *HST* images is R.A.(J2000) = 18:39:53.968, decl.(J2000) = +62:23:34.35. We obtained spectroscopy of this galaxy with the WHT using the Auxiliary Port Camera (ACAM), in observations beginning on 2016 August 22 at 22:57 UT (Levan et al. 2016). The data were reduced using standard IRAF routines. The resulting 2D and 1D extracted spectra are shown in Figure 1, with emission lines of $H\alpha$, $H\beta$, [S II], and [O III] providing a redshift of $z = 0.1616 \pm 0.0002$. The slit was aligned to cross both the nucleus of the main galaxy and a fainter blob of emission to the north, labeled “B” and “C,” respectively, on Figure 2. The latter turned out to be a higher redshift galaxy²³ at $z = 0.4985 \pm 0.0002$, the spectrum of which is also shown in Figure 1.

At a redshift $z = 0.162$ the separation between afterglow and host corresponds to 16.4 kpc in projection, which is consistent with the offset distribution found for other sGRBs (Fong & Berger 2013; Tunnicliffe et al. 2014).

Morphologically, the host appears to be a face-on, disturbed spiral galaxy (Figure 2). The extended, warped appearance of the central bulge suggests an ongoing merger, and the nebular emission lines are consistent with active star formation. It is interesting to note, although most likely coincidental, that the hosts of both sGRB 130603B and GRB 170817A were also notably disturbed (Tanvir et al. 2013; Levan et al. 2017).

The foreground extinction corrected magnitude of the host from the *HST* imaging (with the flux from the $z = 0.5$

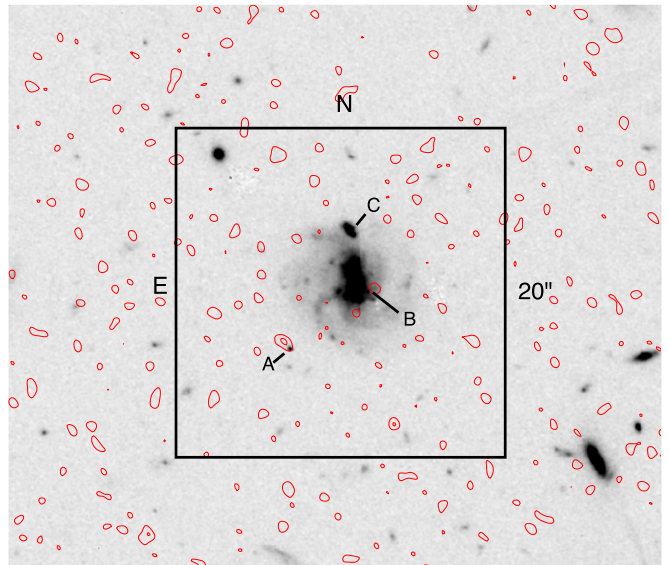


Figure 2. Epoch 1 (3.7 days post-burst) F110W+F160W *HST* image of the field of sGRB 160821B, showing (A) the near-IR counterpart of the burst, (B) the proposed host galaxy at $z = 0.162$, and (C) a background galaxy at $z = 0.5$. The red contours show 1.5σ and 3σ radio flux increments at ~ 10 days post-burst. The slight spatial offset of the radio and optical sources is consistent with the effects of noise in the map.

background galaxy subtracted) is $r_{606,0} = 19.4$. This corresponds to an absolute magnitude of $M_r = -20.0$, which is $\sim L^*/3$ with respect to the Loveday et al. (2015) “blue” (star-forming) galaxy population.

The r -band 25 mag arcsec⁻² isophote has a radius of $\approx 3''.5$, corresponding to a linear scale of ≈ 10 kpc. However, it is possible to trace lower surface brightness emission from the galaxy out to the GRB location, albeit at a faint surface brightness level of ≈ 27 r mag arcsec⁻².

2.4. Further Optical and Near-infrared Monitoring

sGRB 160821B is among the lowest redshift sGRBs found by *Swift* to date. This, combined with its comparatively low foreground Galactic extinction of $A_V = 0.118$ mag (Schlafly & Finkbeiner 2011), motivated an intensive follow-up monitoring campaign.

Further optical and near-IR imaging was obtained with the NOT, the GTC, and the WHT over the next several nights. These data were reduced using standard procedures, and

²³ For completeness, we note that the impact parameter of the GRB from this background galaxy is ≈ 50 kpc, and it has a $P_{\text{chance}} \approx 40\%$, confirming that it is not a good alternative host candidate.

Table 1
Optical and Near-IR Photometry of the sGRB 160821B Afterglow

Δt (day)	t_{exp} (s)	Telescope/Camera	Filter	AB_0	Source of Photometry
0.95	14×300	TNG/DOLoRes	<i>g</i>	24.02 ± 0.16	This work
2.02	7×120	GTC/OSIRIS	<i>g</i>	25.56 ± 0.16	This work
3.98	10×120	GTC/OSIRIS	<i>g</i>	25.98 ± 0.15	This work
6.98	21×120	GTC/OSIRIS	<i>g</i>	26.90 ± 0.18	This work
0.05	6×300	NOT/AIFOSC	<i>r</i>	22.58 ± 0.09	This work
0.07	6×300	NOT/AIFOSC	<i>r</i>	22.52 ± 0.06	This work
0.08	3×90	GTC/OSIRIS	<i>r</i>	22.53 ± 0.03	This work
1.06	6×240	WHT/ACAM	<i>r</i>	23.82 ± 0.07	This work
1.95	9×300	NOT/AIFOSC	<i>r</i>	24.81 ± 0.07	This work
2.03	5×120	GTC/OSIRIS	<i>r</i>	24.80 ± 0.06	This work
3.64	4×621	<i>HST</i> /WFC3/UVIS	F606W	25.90 ± 0.06	This work
4.99	27×120	GTC/OSIRIS	<i>r</i>	26.12 ± 0.25	This work
10.40	4×621	<i>HST</i> /WFC3/UVIS	F606W	27.55 ± 0.11	This work
23.20	1350	<i>HST</i> /WFC3/UVIS	F606W	>27.34	This work
0.08	3×90	GTC/OSIRIS	<i>i</i>	22.37 ± 0.03	This work
2.04	5×90	GTC/OSIRIS	<i>i</i>	24.44 ± 0.10	This work
4.00	3×90	GTC/OSIRIS	<i>i</i>	25.70 ± 0.38	This work
9.97	18×90	GTC/OSIRIS	<i>i</i>	>25.59	This work
0.08	3×60	GTC/OSIRIS	<i>z</i>	22.39 ± 0.02	This work
1.08	6×240	WHT/ACAM	<i>z</i>	23.60 ± 0.15	This work
1.99	9×300	NOT/AIFOSC	<i>z</i>	23.90 ± 0.23	This work
2.04	7×60	GTC/OSIRIS	<i>z</i>	24.34 ± 0.24	This work
3.76	2397	<i>HST</i> /WFC3/IR	F110W	24.69 ± 0.02	This work
10.53	2397	<i>HST</i> /WFC3/IR	F110W	26.69 ± 0.15	This work
23.18	1498	<i>HST</i> /WFC3/IR	F110W	>27.34	This work
0.96	33×20	GTC/CIRCE	<i>H</i>	23.83 ± 0.35	This work
3.71	2397	<i>HST</i> /WFC3/IR	F160W	24.43 ± 0.03	This work
10.46	2397	<i>HST</i> /WFC3/IR	F160W	26.55 ± 0.23	This work
23.23	2098	<i>HST</i> /WFC3/IR	F160W	>27.21	This work
4.3	45×30.8	Keck/MOSFIRE	<i>K</i>	$24.04^{+0.44}_{-0.31}$	Kasliwal et al. (2017a)

Note. Column (1): midtime of observation with respect to GRB trigger time. Magnitudes corrected for Galactic foreground extinction according to $A_V = 0.118$ from Schlafly & Finkbeiner (2011).

calibrated photometrically using Pan-STARRS (optical) and 2MASS (near-IR) stars in the field.

Observations with the *HST* using the Wide Field Camera 3 (WFC3), were obtained in the F606W filter (a wide filter spanning approximately the *V* and *r* bands), the F110W filter (a wide *YJ* band), and the F160W filter (*H* band) from several days to several weeks post-burst (Troja et al. 2016). We adopted the standard photometric calibration for these bands,²⁴ and aperture corrections were determined using bright point sources on the frames.

In all cases, interactive aperture photometry was performed using the *Gaia* software.²⁵ Care was taken to obtain sky estimates close to the position of the transient, because the background was not entirely free of light from the host galaxy.

These observations revealed the counterpart to be initially steady in brightness during the observations made on the first night, but thereafter it faded monotonically in all bands. In the third *HST* visit, at ~ 23 days, no emission is detected at the burst location, which was confirmed by a final visit at ≈ 100 days. A summary of the results of all our optical and near-IR photometry for the sGRB 160821B afterglow, together with selected magnitudes reported elsewhere, is presented in Table 1.

2.5. X-Ray Monitoring

Swift/XRT monitoring continued for 2.5 days, showing evidence for a significant break to a steeper rate of fading around 0.4 days. Our *XMM-Newton* observations comprised two visits at approximately 4 and 10 days post-burst. The first visit produced a very significant detection, and was above a simple extrapolation between the last *Swift* visits. This is discussed further in Section 3.

A summary of the X-ray observations is presented in Table 2.

2.6. Radio Monitoring

The 5 GHz radio detection in 1 hr of observations at 3.6 hr after the burst had a reported flux density of $\sim 35 \mu\text{Jy}$; an additional observation with the same telescope at 26.5 hr post-burst returned a 3σ upper limit of $18 \mu\text{Jy}$ (Fong et al. 2016).

Late-time radio observations of the GRB 160821B field were carried out with the VLA, at a central frequency of about 10 GHz and nominal bandwidth of 4 GHz. The first observation started on 2016 September 1 at 23:24:16 UT; the second observation started on 2016 September 8 at 00:10:33 UT. Data were calibrated using the automated VLA calibration pipeline available in the Common Astronomy Software Applications (CASA). After calibration, data were inspected for flagging, and then imaged using the CLEAN algorithm available in

²⁴ http://www.stsci.edu/hst/wfc3/phot_zp_lbn

²⁵ <http://astro.dur.ac.uk/~pdraper/gaia/gaia.html>

Table 2

Swift (Top) and *XMM-Newton* (Bottom) X-Ray Observations in the 0.3–10 keV Band, of the sGRB 160821B Afterglow after the First Hour

t (day)	0.3–10 keV Flux (10^{-14} erg cm $^{-2}$ s $^{-1}$)
$0.06^{+0.01}_{-0.01}$	$59.6^{+10.8}_{-10.8}$
$0.14^{+0.06}_{-0.02}$	$45.8^{+7.50}_{-7.50}$
$0.30^{+0.03}_{-0.03}$	$32.1^{+9.46}_{-7.45}$
$0.34^{+0.01}_{-0.01}$	$28.0^{+7.42}_{-6.00}$
$0.42^{+0.13}_{-0.02}$	$13.1^{+3.74}_{-2.99}$
$1.02^{+0.39}_{-0.30}$	$3.44^{+1.49}_{-1.10}$
$2.33^{+2.11}_{-0.67}$	≤ 2.53
$3.91^{+0.12}_{-0.12}$	$1.70^{+0.21}_{-0.21}$
$9.95^{+0.17}_{-0.17}$	$0.51^{+0.20}_{-0.20}$

Note. Column (1): times of observation with respect to GRB trigger time, uncertainties represent the duration of the observation. Column (2): fluxes corrected for Galactic foreground absorption following the prescription of Willingale et al. (2013).

CASA. For each of the observations, we estimated the maximum flux density measured within a circular region centered around the position of GRB 160821B and with a radius of $0''.6$ (comparable to the nominal FWHM of the VLA synthesized beam in its B configuration at 10 GHz). If the maximum peak density found within this region is above $3\times$ the image rms, then we report the measured flux density value and assign to it an error obtained by adding in quadrature the image rms and a 5% absolute flux calibration error. On the other hand, if the maximum flux density within the selected circular region does not exceed the $3\times$ rms, we report an upper limit with a value equal to $3\times$ the image rms. Radio data²⁶ are listed in Table 3.

3. Light-curve Behavior, Interpretation, and Modeling

In this section we describe the behavior of the light curve at various observed frequencies. Additionally, we give our interpretation of this behavior before estimating the light curve with physically motivated models. These models provide parameter estimates for the various contributing emission components.

3.1. X-Ray Frequency Light-curve Behavior

A period of extended emission²⁷ (EE) follows the sGRB 160821B prompt emission for a duration of ~ 200 – 300 s. Following the rapid decline of the EE, *Swift*/XRT, and *XMM-Newton* observations show a shallower decline between ~ 0.01 and 10 days; as expected from an afterglow. However, this late-time X-ray flux deviates from the expected power-law decline of a simple afterglow model. The flux level drops below that expected from a power-law decay between ~ 0.3 and 4 days. Rebinning the *Swift*/XRT data into photon bins with a lower minimum count, the behavior of the X-ray light curve is

²⁶ We note that the measured radio flux at ~ 17 days is ~ 31 μ Jy and only just below $3\times$ the image rms. The presented upper limit at this time, <33 μ Jy, is likely an underestimate, where the flux at the GRB location plus 2σ would give a limit of <53 μ Jy.

²⁷ Due to the lack of a clear or consistent definition for extended emission in GRBs, we follow Kisaka & Ioka (2015) who define extended emission as X-ray emission with a duration $\sim 10^2$ s and indicative of a long-lasting central engine. We additionally note that sGRB 160821B is included in the sample of sGRBs with EE by Kisaka et al. (2017) and Kagawa et al. (2019).

Table 3
Radio Data Used in the Analysis

t (day)	ν (GHz)	Flux Density (mJy)	Source
0.15	5.0	0.035	Fong et al. (2016)
1.10	5.0	<0.018	Fong et al. (2016)
10.06	9.8	0.016 ± 0.004	This work
17.09	9.8	<0.033	This work

Note. Column (1): times of observation with respect to GRB trigger time. Column (2): central frequency. Column (3): flux density. Column (4): source, where “This work” refers to observations by the VLA in B configuration under program VLA/16B-386 (PI: Gompertz).

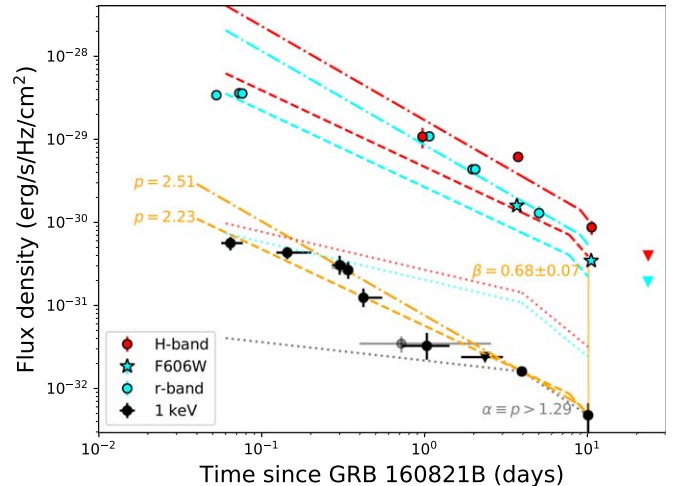


Figure 3. Light curves of the sGRB 160821B afterglow. The X-ray data point horizontal bars represent the duration of the observations, and therefore are not error bars. *Swift*/XRT data from 0.1 to 3 days are rebinned to highlight the steep decline at $\gtrsim 0.3$ days and the low count rate at ~ 2 – 3 days (original binned data are shown as gray symbols); black markers show a detection with associated uncertainty and triangles indicate upper limits. Dashed and dashed-dotted orange lines, representing the limits on a simple power-law afterglow, consistent with the spectral gap between the X-ray and the r -band data at 10 days are shown, see Section 3 for details (we plot F606W data (star symbol) as r -band). A jet break at ~ 7 days is required when assuming this temporal behavior. The r - and H -band optical data are shown in cyan and red, respectively, with a power-law light curve extrapolated from the dashed/dashed-dotted X-ray limits. Ignoring the optical to X-ray spectral constraints, the minimum power-law permitted by the late X-ray data, i.e., assuming a jet-break at ~ 4 days, is shown as a dotted gray line at 1 keV and extrapolated to the expected r - and H -band afterglow in cyan and red.

more clearly revealed; see Figure 3 where the gray markers show the data using the typical minimum photon count per bin and the black markers show the rebinned flux levels (a triangle indicates an upper limit). A photon index $\Gamma = 1.7$ is assumed, which is consistent with both *Swift*/XRT ($\Gamma = 2.0^{+0.7}_{-0.6}$) and *XMM-Newton* ($\Gamma = 1.4^{+0.5}_{-0.4}$). Horizontal error bars indicate the duration of the observations at each point. The rebinned data reveal a break in the X-ray light curve at ~ 0.35 days, where the flux drops significantly for all the following data, and the flux level at 2–3 days is comparable to the *XMM-Newton* observed flux level at ~ 4 days.

3.2. Behavior at Optical and Near-infrared Frequencies

Figure 4 shows the spectral energy distribution of all the optical data from Table 1, where we have averaged together

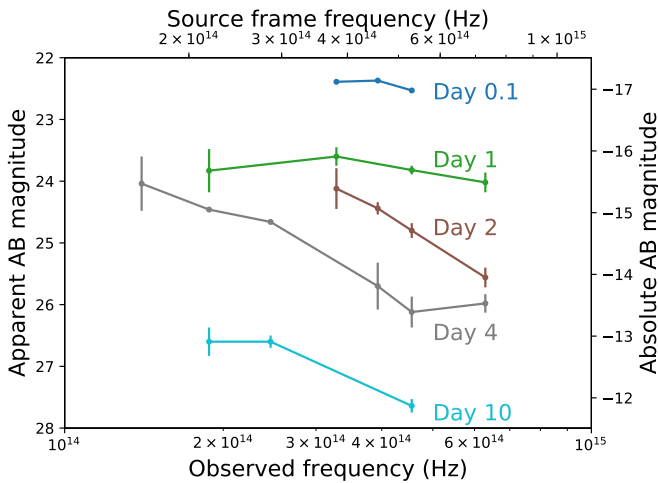


Figure 4. Spectral energy distribution of the transient at five epochs, illustrating the large changes in color, from blue to red. The photometry has been corrected for foreground Galactic extinction.

points taken in the same filter at close to the same time. The color evolution of the transient exhibits a trend from blue in observations taken roughly one day after the burst to a much redder color in all subsequent detections. This is immediately indicative of an emerging kilonova component; which itself is evolving from blue to red on timescales of days (see, e.g., Perego et al. 2014; Tanaka et al. 2018; Wollaeger et al. 2018). r - and H -band data are shown in Figure 3 for comparison with a typical power-law decline extrapolated from the power law used to show the behavior at X-ray frequencies (see Section 3.1). The deviation from a power law with an excess in blue and then red is evident; the behavior at optical and near-IR is distinct from that at 1 keV.

We note that while treating the F606W magnitudes as r -band in principle introduces a systematic error, the measured g -F606W color is flat (consistent with our interpretation below that the optical light is afterglow dominated at these times), indicating that color corrections would be smaller than the photometric errors. (Furthermore, even for our kilonova models, at the time of those epochs, the predicted difference between F606W and the r -band is $\lesssim 0.2$ AB mag.)

3.3. At Radio Wavelengths

Radio observations show a fading source between ~ 0.1 and 1 day, but a detection at ~ 10 days indicates continued radio afterglow emission as shown by the red contours in Figure 2 (note that the small apparent offset between the radio and optical positions is consistent with the effects of noise in the radio map, given the low S/N). The late afterglow is limited by a nondetection at ~ 17 days.

3.4. Interpretation

A kilonova component is likely to peak in the optical within one to two days post-merger, leading us to expect the r -band flux to be dominated by afterglow at the early (~ 0.1 days) and late (~ 10 days) epochs. Inspection of the spectral energy distribution at ~ 0.1 days between the X-ray (1 keV) and the r -band optical data reveals $\beta = 0.66 \pm 0.03$, where $F_\nu \propto \nu^{-\beta}$, and is consistent with $\beta = 0.68 \pm 0.07$ at ~ 10 days in agreement with this expectation (see Figure 3). Using the broader spectral index limits at ~ 10 days, and assuming a

temporal decline as $F_\nu \propto t^{-\alpha}$, where $\alpha = 3(p-1)/4$, the power-law behavior for the limits on p from $p = 2\beta + 1$ is shown. A break in the light curve at $t_j \sim 7$ days is required, where $\alpha = -p$ at $t > t_j$; this break will be achromatic. The X-ray light curve drops significantly below the lower limit ($p = 2.23$) power-law extrapolated to earlier times from ~ 4 days.

The X-ray light curve exhibits an earlier break at $t \sim 0.35$ days, and a late-time excess. Afterglow variability is discussed in Ioka et al. (2005), and such an excess is expected from either a refreshed shock where a slower shell catches up with the initial decelerating outflow (e.g., Panaitescu et al. 1998; Zhang & Mészáros 2002), or a structured jet with an angle-dependent energy and Lorentz factor distribution (e.g., Lamb & Kobayashi 2017). By assuming the jet structures used to model the afterglow to GRB 170817A in Lamb et al. (2019), where on axis the resultant GRB would have been consistent with the short GRB population (e.g., Salafia et al. 2019), then from the observed γ -ray energy of GRB 160821B we can estimate the system inclination following Ioka & Nakamura (2019). For a Gaussian structure with GRB 170817A-like core energy [$\log_{10}(E_c) = 52.4^{+0.4}_{-0.5}$], then to reproduce the prompt γ -ray energy of GRB 160821B, the system should be inclined at $\sim \theta_c + (3 \pm 2)^\circ$ (see also Troja et al. 2019); for a two-component jet [$\log_{10}(E_c) = 52.0^{+0.6}_{-0.9}$] then the opacity of the low- Γ second component must be considered (e.g., Lamb & Kobayashi 2016) and the expected inclination would be $\sim \theta_c + (1.5 \pm 1.5)^\circ$. For a structured jet, however, a late-time rebrightening in the afterglow is only expected for some structure profiles and at higher inclinations, $\sim (3-5) \times \theta_c$ ²⁸ where bright γ -ray emission is not expected (see Lamb & Kobayashi 2017, 2018; Gill & Granot 2018; Beniamini & Nakar 2019; Matsumoto et al. 2019). Considering the bright GRB we assume that GRB 160821B is on axis or very close to on axis, where the resultant afterglow would behave similarly to the on-axis case regardless of the jet structure (see Lamb & Kobayashi 2017). For our working model we favor a refreshed shock scenario with two shells where $\Gamma_1 > \Gamma_2$, here the subscript indicates the shell order. If the jet breaks at $t \sim 0.35$ days, then the apparent break at $t > 4$ days is indicative of a turnover in the light curve following a significant energy injection episode.

The extended emission at X-ray frequencies lasting until $\sim 200-300$ s post sGRB 160821B supports continued engine activity beyond the timescale of the GRB. This X-ray emission is consistent with an outflow episode driven by fallback accretion onto a spinning black hole (Rosswog 2007; Metzger et al. 2008; Nakamura et al. 2014; Kisaka & Ioka 2015; Yu et al. 2015; Kisaka et al. 2017). A peak or break time of ~ 4 days for the refreshed shock indicates that the bulk Lorentz factor of the outflow when the second shell catches the first should be low, with $\Gamma(t) \sim 10$ and the second shell will have a Lorentz factor much lower than the value typically expected for a successful GRB, $\Gamma_2 \ll 100$. Energy dissipated within a low- Γ outflow is not expected to be emitted at γ -ray energies; γ -rays injected into the outflow will be coupled to the plasma and these photons will adiabatically cool and thermalize due to scattering. The effect of these processes is to suppress any resulting emission, which will have a spectral peak at \sim X-ray frequencies. Photons that fail to escape from a low- Γ jet will be

²⁸ A late excess/rebrightening is not expected from a Gaussian profile structure.

reabsorbed by the outflow and contribute to the jet kinetic energy driving the afterglow (Kobayashi & Sari 2001; Kobayashi et al. 2002; Lamb & Kobayashi 2016). The energy-loss by the photon distribution and reabsorption by the outflow will result in a very low value for the emission efficiency, η . This low- Γ X-ray extended emission producing shell follows the initial, high- Γ , GRB producing shell, which will decelerate as $\Gamma_1(t) \propto t^{-3/8}$ as it sweeps-up the ambient medium. However, the second shell encounters very little material and will catch up with the forward shell when $\Gamma_1(t) \sim \Gamma_2/2$ (Kumar & Piran 2000). The energy of the second shell refreshes the forward shock resulting in a rebrightening of the afterglow (e.g., Granot et al. 2003).

Although limited, the observations at radio frequencies place tight constraints on any possible afterglow, and the afterglow parameters will be constrained by the detection and upper limits at 1–10 days. The early radio detection at ~ 0.1 days, brighter than the following upper limits and flux at ~ 10 days, is likely the result of a reverse shock (e.g., Mészáros & Rees 1997; Sari & Piran 1999; Kobayashi 2000; Kobayashi & Sari 2001; Resmi & Zhang 2016; Lamb & Kobayashi 2019). Given the X-ray to optical spectral index $\beta \sim 0.66$, the 5 GHz radio emission at ~ 0.1 days is below the characteristic synchrotron frequency ν_m ; if the ~ 0.1 day radio emission at 5 GHz belongs to the forward shock, then as $F_{5\text{ GHz}} = F_{\nu, \text{max}}(\nu_R/\nu_m)^{1/3}$ and considering the flux at X-ray frequencies is $F_X = F_{\nu, \text{max}}(\nu_X/\nu_m)^{-\beta}$, then $\nu_m \sim 6.4 \times 10^{14} (F_X/F_{5\text{ GHz}})^{-1}$ Hz giving $\nu_m \sim 10^{12}$ Hz. As $\nu_m \propto t^{-3/2}$ and t^{-2} for the afterglow before and after the jet break, the 5 GHz radio emission will brighten until a peak when $\nu_m = 5$ GHz or the jet breaks; in either case, the upper limit of $18 \mu\text{Jy}$ at ~ 1 day post sGRB 160821B rules out the earlier detection being due to the forward shock. This is the first successfully modeled candidate of a reverse shock in an unambiguous sGRB afterglow and indicates that, in some cases, emission from the reverse shock can be bright despite previous nondetections (Lloyd-Ronning 2018; however, see Becerra et al. 2019 where a reverse shock was recently claimed for the candidate short GRB 180418A). Any afterglow model that can explain the behavior at X-ray frequencies and the early and late optical and near-IR should also be consistent with the detection and limits at radio frequencies.

The afterglow at both radio and X-ray frequencies can constrain the behavior at optical and near-IR. These observations indicate an excess in blue at early times followed by a reddening; this behavior is indicative of a kilonova. Previous studies of sGRB 160821B have been restricted to much smaller photometric data sets and consequently have only drawn weak conclusions about the possibility of a kilonova component and the nature of the afterglow (Kasliwal et al. 2017a; Gompertz et al. 2018; Jin et al. 2018). Here, we use the X-ray, early optical and radio constraints on the afterglow emission to interpret the kilonova contribution at optical and near-IR frequencies. We use the latest kilonova light-curve models based on numerical-relativity simulations to constrain the dynamical and post-merger ejecta masses (e.g., Kawaguchi et al. 2018).

3.5. Afterglow Modeling

We use the analytic solution for a relativistic blast wave from Pe'er (2012), and the method for generating afterglow light curves from Lamb et al. (2018) to estimate the broadband

afterglow for a given set of parameters. We use the observed data to constrain several of the GRB afterglow parameters. As the optical flux at ~ 10 days could still have some kilonova contribution, we use the 1 keV to r -band spectral slope at ~ 0.05 days to estimate p , where $\beta \sim 0.66$ giving $p = 2.3$. If we assume a prompt efficiency of $\eta \sim 0.1\text{--}0.15$ (Fong et al. 2015), then the isotropic equivalent kinetic energy in the initial outflow is $E_{k, \text{iso}} \sim (1\text{--}2) \times 10^{51}$ erg. Throughout, we fix $\varepsilon_B = 0.01$ for the forward shock, consistent with the range for short GRBs (Fong et al. 2015).

The optical flux is approximately flat between 0.05 and 0.07 days; this flatness combined with a likely reverse shock in the radio at the same time indicates that these points coincide with the deceleration timescale for the outflow. By fixing the ambient density to $n = 10^{-4} \text{ cm}^{-3}$, consistent with the location in the outskirts of the host galaxy (see Figure 2), the Lorentz factor of the GRB outflow can be estimated; $\Gamma_0 \sim 18 [t_d/(1+z)]^{-3/8} (E_{k, \text{iso}}/10^{51} \text{ erg})^{1/8} (n/10^{-4} \text{ cm}^{-3})^{-1/8} \sim 55\text{--}60$, where $t_d \sim 0.06$ days is the deceleration time. Similarly, the break at $t_j \sim 0.35$ days can be used to estimate the jet half-opening angle, $\theta_j \sim 0.05 [t_j/(1+z)]^{3/8} (E_{k, \text{iso}}/10^{51} \text{ erg})^{-1/8} (n/10^{-4} \text{ cm}^{-3})^{1/8} \sim 0.033$ rad, or $\sim 1.9^\circ$. As the break time dominates the opening angle estimation, we can put weak limits on this value of $1.9^{+0.10}_{-0.03}$ degrees (these small errors are only the formal fit uncertainty given this choice of jet model and decomposition of the light curve; the systematic errors from uncertainties in the model assumptions are much greater, and poorly quantifiable), this narrow jet is consistent with the opening angle range for short GRBs (Jin et al. 2018).

The forward shock is refreshed at ~ 1 day, peaking at ~ 3 days and then declining as $\sim t^{-p}$. We assume that the second shell has the same half-opening angle as the first. As the jet has broken, sideways expansion could widen the initial blast wave and the second shell will only refresh the blast wave with an opening angle $\leq \theta_j$. By assuming that the radius of the blast wave is roughly constant after the jet break²⁹ then the Lorentz factor of the second shell is

$$\Gamma_2 \gtrsim 47.4 \left(\frac{1+z}{t_c} \right)^{1/2} \left(\frac{E_{k, \text{iso}}}{10^{51} \text{ erg}} \right)^{1/6} \left(\frac{n}{10^{-4} \text{ cm}^{-3}} \right)^{-1/6} \theta_j^{1/3}, \quad (1)$$

where $\Gamma_2 \gtrsim 16$ for an observed collision time $t_c \sim 1$ day. The Lorentz factor of the forward shock at the collision is then $\Gamma_1(t) \gtrsim 8$.

We find that if the forward shock is refreshed when $\Gamma_1(t) = 12$ and the resulting blast wave has $12.5 \times E_{k, \text{iso}}$ of the initial outflow energy then the afterglow can account for the X-ray excess at ~ 4 days. The radio afterglow at ~ 10 days constrains the microphysical parameter $\varepsilon_e \sim 0.3$, so as not to overproduce the radio flux. We assume throughout that the initial and final blast wave have identical microphysical parameters ε_B and ε_e , electron index p , and θ_j .

The early radio point at ~ 0.1 days requires a significant reverse shock. For this point to be forward shock dominated the X-ray and optical data constrain the characteristic synchrotron frequency to $\nu_m \sim 10^{12}$ Hz, much lower than the model estimate of $\nu_m \sim 3.5 \times 10^{14}$ Hz. As $\nu_m \propto \Gamma^4 \varepsilon_B^{1/2} n^{1/2} \varepsilon_e^2$, then the parameters that can successfully explain the X-ray and

²⁹ The sideways expansion does not halt the radial progress of the jet (Granot & Piran 2012; Lamb et al. 2018); by assuming that it does, we can place a lower limit on the Lorentz factor of the second shell.

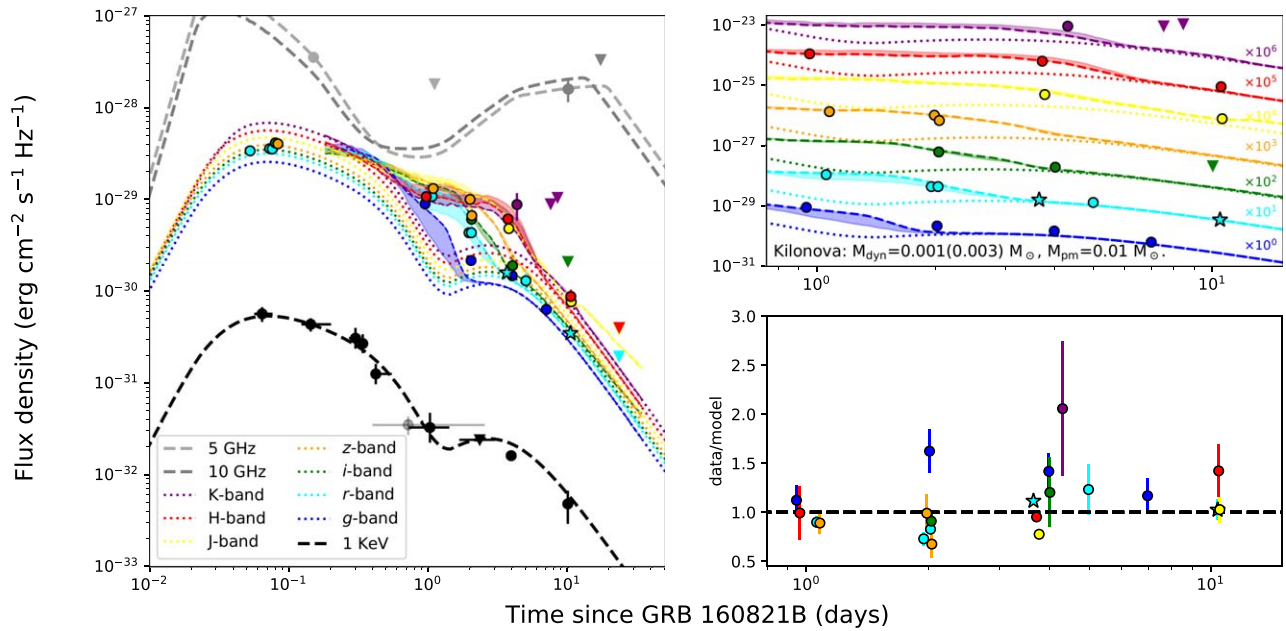


Figure 5. Left panel: X-ray, optical, near-infrared, and radio frequency observations of sGRB 160821B afterglow. Star markers in the r -band indicate *HST*/WFC/F606W data points. Errors are 1σ and upper limits are shown as triangles. Overplotted are the afterglow light curves for a two episode jet and afterglow plus kilonova light curves between 0.1 and 30 days, as described in the text. The reverse shock is dominant at $\lesssim 1$ day at 5 GHz (light gray dashed line). The rebinned *Swift*/XRT and *XMM-Newton* data (black markers) show the complex behavior of the afterglow indicative of a two episode outflow. The optical data are clearly in excess above the afterglow model (dotted lines) in blue to red between ~ 1 and 5 days. The afterglow plus the preferred kilonova model are shown as colored dashed lines where the shaded region indicates the parameter space for a dynamical mass in a range of 0.001 – $0.003 M_{\odot}$, where a higher dynamical mass reduces the g -band flux at ~ 1 day and increases the K -band flux at ~ 4 days. Top right: zoom plot of the optical to near-IR. The in-band light curves are separated by the factor indicated for each line. Afterglow is shown as dotted lines and the sum of the afterglow model and the kilonova model is shown as dashed lines. Bottom right: the residual of the best fitting afterglow plus kilonova model and the data. The line and marker colors for each band are given in the legend.

optical afterglow would need significantly lower values. Such lowered parameter values result in an afterglow that is inconsistent with the other observations and unphysical parameters in many cases. Following Harrison & Kobayashi (2013), the characteristic synchrotron frequency ν_m and the maximum flux $F_{\nu, \max}$ for the reverse shock can be found from the forward shock parameters. The reverse shock flux before and after the peak will scale following Kobayashi (2000); for the thin shell case and our parameters, the flux pre-peak will scale as $F_{\nu} \propto t^{5.7}$ and post peak $F_{\nu} \propto t^{-2.05}$. To accommodate the early radio detection, we need to use a magnetization parameter of $R_B \sim 8$. The model light curve is shown in Figure 5, where we have taken an initial kinetic energy of $E_{k, \text{iso}} = 1.3 \times 10^{51}$ erg and $\theta_j = 0.033$, with all other parameters as discussed.

3.6. The Kilonova Modeling

The kilonova appears as an excess in the optical above the afterglow. From Figure 5, where the optical afterglow is shown as dotted lines, it is clear that all bands are in excess at ~ 1 day post-burst. The bluer bands (g , r , and i) follow the afterglow from ~ 5 days while the redder bands (J , H , and K) remain in excess until ~ 10 days post GRB.

Using two-component kilonova models from Kawaguchi et al. (2018), K -corrected to $z = 0.16$, we find the model parameters via a χ^2 minimization fit to the data for the kilonova plus model afterglow. The kilonova is best described³⁰ by a secular ejecta (or post-merger wind driven by viscous and neutrino heating) with a mass $M_{\text{pm}} = 0.01 M_{\odot}$, and a dynamic

ejecta mass $M_{\text{dyn}} = 0.001 M_{\odot}$. The density profile for each ejecta component is given by

$$\rho(r, t) \propto \begin{cases} r^{-3} t^{-3} & 0.025c \leq r/t \leq 0.15c, \\ r^{-6} \zeta(\theta) t^{-3} & 0.15c \leq r/t \leq 0.9c. \end{cases} \quad (2)$$

Here the top condition is for the secular ejecta, and the bottom condition for the dynamic ejecta. We find good fits for an upper limit for the secular ejecta velocity, and lower limits for the dynamic ejecta velocity, of 0.1 – $0.15c$. The function $\zeta(\theta)$ describes the angular distribution of the dynamic ejecta, and is given by

$$\zeta(\theta) = 0.01 + \frac{0.99}{1 + e^{-20(\theta - \pi/4)}}, \quad (3)$$

where θ is the angle from the central axis.

The element abundances for the ejecta are determined following the results of r -process nucleosynthesis calculations by Wanajo et al. (2014) and assuming that the secular and dynamic ejecta have initially flat electron fraction Y_e distributions ranging from 0.3 to 0.4 and from 0.1 to 0.4, respectively. Radiative transfer simulations were performed from 0.1 to 30 days resulting in a light curve with a statistical error in each band ~ 0.1 – 0.2 mag.

The kilonova fit to the data depends on the afterglow subtraction, however, the precise details of the afterglow parameters are not crucial. As the optical afterglow is typically in the same spectral regime as the observed X-ray data for sGRBs, and supported by the similar spectral index between optical and X-rays at 0.1 and 10 days, then the optical afterglow will follow that at X-ray frequencies during the kilonova peak. The X-ray data extrapolated to the optical at ~ 1 – 4 days

³⁰ The models have masses drawn from the parameter grid $M_{\text{dyn}} = [0.001, 0.002, 0.003, 0.005, 0.01] M_{\odot}$, and $M_{\text{pm}} = [0.01, 0.02, 0.03, 0.05, 0.1] M_{\odot}$.

post-burst indicates that the afterglow contributes $\sim 10\%$. The typical photometric uncertainty is $\sim 10\%$, and the kilonova model uncertainty is $\sim 10\%$. Combining these uncertainties, and using the analytic scaling for luminosity with mass $L \propto M^{0.35}$ (e.g., Grossman et al. 2014), we can give limits on the mass estimates from the kilonova model fit of $\sim \pm 60\%$; however, we emphasize that both the masses and the uncertainties are model specific.

4. Discussion

We have shown that the afterglow of sGRB 160821B with extended X-ray emission until ~ 300 s post-burst exhibits a reverse shock at early times and a refreshed shock at late times. Early time observations at radio wavelengths require a reverse shock, while the complex light curve at X-ray frequencies observed by *Swift*/XRT and *XMM-Newton*, combined with late-time radio observations reveal a break at ~ 0.35 days and a rebrightening at > 1 day. The jet is very narrow, at $\theta_j \sim 1^\circ.9$, and the slower second outflow episode that refreshes the forward shock carries significantly more energy than the initial outflow. However, the total combined energy of the jets, $E_j \sim 0.9 \times 10^{49}$ erg, is consistent with the short GRB population (Fong et al. 2015).

Extended emission can be the result of a magnetar (e.g., Fan & Xu 2006; Metzger et al. 2008; Bucciantini et al. 2012; Gompertz et al. 2013; Gibson et al. 2017), or energy dissipated within a jet launched due to mass fallback onto the central compact object (Fan et al. 2005; Rosswog 2007; Kisaka & Ioka 2015; Kisaka et al. 2017); see also Barkov & Pozanenko (2011) for a two-component jet model. The refreshed shock at late times requires a second episode of jet activity and fallback accretion onto the central compact object supports both this late-time rebrightening and the extended emission. From the afterglow modeling, the second jet episode has a Lorentz factor of $\Gamma_2 \sim 24$. Internal energy dissipation within such a low- Γ jet is expected to be suppressed due to a large optical depth, see Lamb & Kobayashi (2016); however, any resulting emission will peak at X-ray frequencies and have a longer timescale than the initial dissipation timescale. Considering the energy required to refresh the forward shock, the efficiency of energy dissipation within the fallback launched jet is $\eta \sim 10^{-3}$, consistent with the expectation from a low- Γ outflow (Lamb & Kobayashi 2016). The fallback mass required to launch such an energetic second outflow can be estimated following Kisaka et al. (2017) giving a mass $\sim 2 \times 10^{-3} M_\odot$.

As well as the EE and the refreshed shock, the afterglow reveals a reverse shock (the first confirmed reverse shock in an sGRB, see Lloyd-Ronning (2018), who highlight the lack of observed reverse shocks in sGRBs); such a shock propagates into the colder and denser inner shell. To recreate the reverse shock emission, we follow Lamb & Kobayashi (2019) and require a magnetization parameter of $R_B \sim 8$. Thus the magnetic field within the shell is much larger than the magnetic field induced by the forward shock. A high magnetic field indicates that the shell is endowed with primordial magnetic fields from the central engine.

In addition to these afterglow features, a kilonova is present at optical and near-IR frequencies. The best fitting model is one represented by a dynamic ejecta mass of $\sim 0.001 M_\odot$ and a secular ejecta mass $\sim 0.01 M_\odot$. The secular ejecta mass, required for the early blue excess, is consistent with the expectation of the mass-loss from a torus surrounding a

massive neutron star (Fujibayashi et al. 2018; Fernández et al. 2019). However, the best-fit model from our parameter sample under-predicts the observed g -band emission at ~ 2 and ~ 4 days post-burst, this is likely due to the finite parameter spacing of the kilonova model samples. A small secular ejecta mass $\sim 0.01 M_\odot$ and the low dynamic ejecta mass $\sim 0.001 M_\odot$ may indicate that the remnant collapses to a black hole promptly after the merger (Kiuchi et al. 2009; Sekiguchi et al. 2016; Coughlin et al. 2018; Radice et al. 2018). In such a scenario the electron fraction, Y_e , will be lower. To test this, we compared the kilonova light curve of the best-fit model with a model using a lower electron fraction distribution for the post-merger wind $Y_e = 0.1\text{--}0.3$ as expected from a prompt collapse scenario. A comparison of the light curves for these two scenarios was performed, the results indicate that the prompt collapse to a black hole, with a low- Y_e and a higher velocity, will overproduce the red excess at late times and underproduce the early blue excess; see Figure 6. Thus, the observed blue emission in the early phase suggests the existence of a low opacity component, when interpreted as kilonova emission, and we can conclude that a very prompt collapse to a black hole is unlikely to explain the observed transient when considering the observed features. Note that the afterglow subtracted data at $\gtrsim 4$ days is typically brighter than the kilonova model we use, especially at K -, J -, r -, and g -bands. This excess at bluer wavelengths is due to the afterglow subtraction, where the emission is afterglow dominated and the model afterglow slightly underpredicting the observed flux. The observed K - and J -band excesses (~ 4 and ~ 10 days post-burst) have large associated errors, and the best-fit model is within 2σ of each detection without considering the model uncertainty (see Figure 5).

Of the five widely discussed GRBs with candidate kilonova contributions to their light curves—GRBs 050709, 060614, 070809, 130603B, and 150101B (Yang et al. 2015; Jin et al. 2016, 2019; Gompertz et al. 2018; Troja et al. 2018)—the kilonova in sGRB 160821B is the best sampled. At $\sim 0.011 M_\odot$, the kilonova in sGRB 160821B has an ejecta mass toward the lower end of the range proposed for any of these other cases, and is consistent with the $< 0.03 M_\odot$ found by Kasliwal et al. (2017a). The kilonova following GW170817 had an ejecta mass $\sim 0.03\text{--}0.05 M_\odot$ (e.g., Pian et al. 2017; Smartt et al. 2017), similar to the mass estimates for sGRB 130603B, $\sim 0.03 M_\odot$ (e.g., Jin et al. 2016), whereas, GRB 050709, 060614, 070809, and 150101B have masses $\sim 0.05, 0.13, 0.015,$ and $< 0.004 M_\odot$ respectively (Yang et al. 2015; Jin et al. 2016). However, we note that upper limits implied by kilonova nondetection in some other sGRBs could indicate the existence of fainter kilonovae indicating still lower ejecta masses³¹ (e.g., Gompertz et al. 2018).

The best-fit kilonova model is consistent with the scenario where, following the merger, a massive neutron star survives for a short period (Fujibayashi et al. 2018). This scenario is similar to the case of GRB 170817A, for which various arguments point to a short-lived massive neutron star (e.g.,

³¹ The heating rates and therefore the estimated masses depend on the chosen nuclear mass formula (e.g., Barnes et al. 2016; Rosswog et al. 2017). For the very low Y_e ejecta the r -process path passes close to the neutron-dripline in the nuclear chart, this is experimentally uncharted territory, and we rely on purely theoretical mass formulae. The amounts of trans-lead nuclei, important because they are efficient in releasing energy and their decay products are efficiently thermalizing with the ambient medium, depend quite sensitively on the chosen mass formula

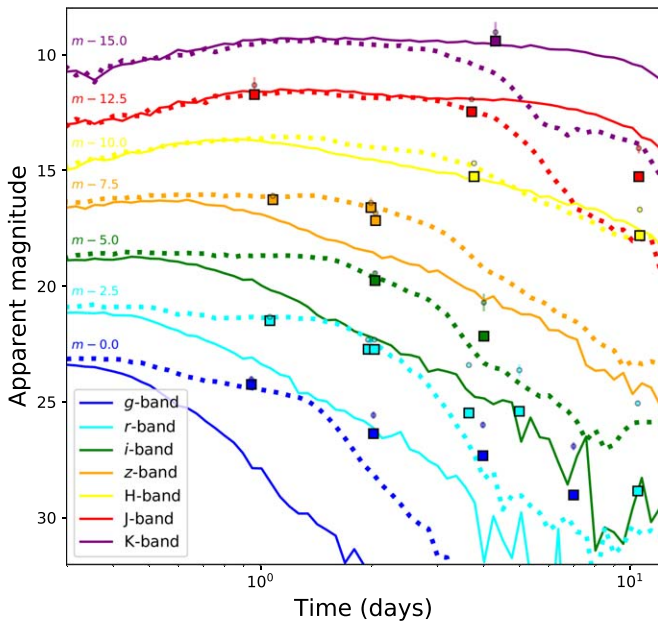


Figure 6. Kilonova model light curves for a BNS to a short-lived hypermassive neutron star (the model used by our analysis) is shown as dotted lines, compared to the scenario where the BNS promptly forms a black hole, shown as solid lines. The in-band flux has been separated by a factor, annotated on each light curve. The square markers show the data with the model afterglow flux removed, the original data are shown with error bars and a small circle. The prompt collapse scenario underproduces the early, $\lesssim 4$ days, bluer observations.

Margalit & Metzger 2017; Ai et al. 2018; Pooley et al. 2018, see Piro et al. 2019 for an alternative interpretation); however, the lower ejecta mass in sGRB 160821B could point to a more rapid collapse of the remnant massive neutron star. Extended emission was present in sGRB 160821B and is used to argue for significant mass fallback in this case, however, for GRB 170817A *Swift*/XRT did not begin observations until ~ 15 hr after the initial burst (Evans et al. 2017) and any EE would have long faded. The total energy in the jets in sGRB 160821B is lower than the energy required to drive the afterglow to GRB 170817A and, additionally, the required outflow structure is very different (e.g., Lamb et al. 2019). These differences, combined with the lower mass of the ejecta in sGRB 160821B when compared to GRB 170817A, could offer some clue as to the dynamical differences between mergers and sGRB phenomena. Understanding these differences may help explain the diversity in sGRB properties; especially among systems with a similar progenitor, i.e., BNS mergers.

5. Conclusions

We have reported ground- and space-based optical and near-infrared monitoring of sGRB 160821B. We see clear evidence for red to blue evolution in the color of the transient, indicative of a kilonova. The data set presented here makes the kilonova in sGRB 160821B the best-sampled kilonova without a coincident gravitational wave signal. We find that a kilonova model with a dynamic ejecta mass $M_{\text{dyn}} \sim 0.001 M_{\odot}$, a velocity distribution $(0.15\text{--}0.9)c$, and a flat electron fraction distribution $Y_e = 0.1\text{--}0.4$; and a secular ejecta with $M_{\text{pm}} \sim 0.01 M_{\odot}$, a velocity distribution $(0.025\text{--}0.15)c$, and $Y_e = 0.3\text{--}0.4$ can best explain the observed emission, while the mass estimates have $\sim 60\%$ uncertainty. The blue excess, the mass of the dynamic and

secular ejecta, and the electron fraction supports the existence of a short-lived massive neutron star that does not immediately collapse to a black hole.

We have also presented *Swift* and *XMM-Newton* observations of the event and combining with constraints from VLA radio observations find a complex afterglow with a radio-emitting reverse shock into a magnetized shell and a late-time, broadband, refreshed shock. The jet is very narrow with $\theta_j \sim 1.9^\circ$, and the second episode is significantly more energetic than the first. We find the prompt and extended emission, plus the early- and late-time rebrightening afterglow to be consistent with multiple accretion episodes onto the central compact object with the second episode consistent with a fallback mass of $\sim 0.002 M_{\odot}$.

The authors thank the anonymous referee for helpful and constructive comments. GPL additionally thanks Alice Breeveld, Kunihito Ioka, Geoff Ryan, Graham Wynn, and Tomos Meredith for useful discussions and Yizhong Fan for helpful comments. We thank A. Melandri (INAF/OABr) for help in the preparation of the TNG observation.

Partly based on observations made with the Gran Telescopio Canarias (GTC), installed in the Spanish Observatorio del Roque de los Muchachos of the Instituto de Astrofísica de Canarias, in the island of La Palma; and with the Nordic Optical Telescope, operated by the Nordic Optical Telescope Scientific Association at the Observatorio del Roque de los Muchachos (program 51–504); and with the Italian Telescopio Nazionale Galileo (TNG) operated by the Fundación Galileo Galilei of the INAF (Istituto Nazionale di Astrofisica) at the Spanish Observatorio del Roque de los Muchachos (program A32TAC_5). The development of CIRCE at GTC was supported by the University of Florida and the National Science Foundation (grant AST-0352664), in collaboration with IUCAA. Based on data from the GTC Public Archive at CAB (INTA-CSIC).

This work has made use of data from the European Space Agency (ESA) mission *Gaia* (<https://www.cosmos.esa.int/gaia>), processed by the *Gaia* Data Processing and Analysis Consortium (DPAC, <https://www.cosmos.esa.int/web/gaia/dpac/consortium>). Funding for the DPAC has been provided by national institutions, in particular, the institutions participating in the *Gaia* Multilateral Agreement.

N.R.T., A.J.L., K.W., and B.G. have received funding from the European Research Council (ERC) under the European Union’s Horizon 2020 research and innovation programme (grant agreement No. 725246, TEDE, PI Levan).

A.J.L. and J.D.L. acknowledge support from STFC via grant ST/P000495/1.

N.R.T. and G.P.L. acknowledge support from STFC via grant ST/N000757/1.

E.P. acknowledges support from grant ASI/INAF I/088/06/0.

J.H. was supported by a VILLUM FONDEN Investigator grant (project number 16599).

D.B.M. acknowledges support from the Instrument center for Danish astrophysics (IDA).

The National Radio Astronomy Observatory is a facility of the National Science Foundation operated under cooperative agreement by Associated Universities, Inc. A.C. acknowledges support from the National Science Foundation CAREER award #1455090.

A.d.U.P., C.C.T., Z.C., L.I., and D.A.K. acknowledge support from the Spanish research projects AYA2014-58381-P and AYA2017-89384-P, from the State Agency for Research of the Spanish MCIU through the “Center of Excellence Severo Ochoa” award for the Instituto de Astrofísica de Andalucía (SEV-2017-0709). A.d.U.P. and C.C.T. acknowledge support from Ramón y Cajal fellowships (RyC-2012-09975, and RyC-2012-09984). Z.C., L.I., and D.A.K. acknowledge support from Juan de la Cierva Incorporación fellowships (JdCI-2014-21669, IJCI-2016-30940, and IJCI-2015-26153).




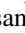














P.A.E. and K.L.P. acknowledge support from the UK Space Agency.

K.E.H. and P.J. acknowledge support by a Project grant (162948–051) from The Icelandic Research Fund.

S.R. has been supported by the Swedish Research Council (VR) under grant No. 2016-03657_3, by the Swedish National Space Board under grant No. Dnr 107/16 and by the research environment grant “Gravitational Radiation and Electromagnetic Astrophysical Transients (GREAT)” funded by the Swedish Research council (VR) under Dnr 2016-06012.

Facilities: GTC(OSIRIS/CIRCE), *HST*(WFC3), NOT (ALFOSC), *Swift*(XRT and BAT), TNG(DOLORES), VLA, WHT(ACAM).

ORCID iDs

G. P. Lamb  <https://orcid.org/0000-0001-5169-4143>
 N. R. Tanvir  <https://orcid.org/0000-0003-3274-6336>
 A. Corsi  <https://orcid.org/0000-0001-8104-3536>
 D. B. Malesani  <https://orcid.org/0000-0002-7517-326X>
 K. L. Page  <https://orcid.org/0000-0001-5624-2613>
 K. Wiersema  <https://orcid.org/0000-0002-9133-7957>
 M. Shibata  <https://orcid.org/0000-0002-4979-5671>
 M. Tanaka  <https://orcid.org/0000-0001-8253-6850>
 A. J. van der Horst  <https://orcid.org/0000-0001-9149-6707>
 Z. Cano  <https://orcid.org/0000-0001-9509-3825>
 J. P. U. Fynbo  <https://orcid.org/0000-0002-8149-8298>
 J. Hjorth  <https://orcid.org/0000-0002-4571-2306>
 L. Izzo  <https://orcid.org/0000-0001-9695-8472>
 D. A. Kann  <https://orcid.org/0000-0003-2902-3583>
 D. A. Perley  <https://orcid.org/0000-0001-8472-1996>
 E. Pian  <https://orcid.org/0000-0001-8646-4858>
 D. Watson  <https://orcid.org/0000-0002-4465-8264>
 R. A. M. J. Wijers  <https://orcid.org/0000-0002-3101-1808>

References

- Abbott, B. P., Abbott, R., Abbott, T. D., et al. 2017a, *ApJL*, **848**, L12
 Abbott, B. P., Abbott, R., Abbott, T. D., et al. 2017b, *ApJL*, **848**, L13
 Ai, S., Gao, H., Dai, Z.-G., et al. 2018, *ApJ*, **860**, 57
 Andreoni, I., Ackley, K., Cooke, J., et al. 2017, *PASA*, **34**, e069
 Ascenzi, S., Coughlin, M. W., Dietrich, T., et al. 2019, *MNRAS*, **486**, 672
 Barkov, M. V., & Pozanenko, A. S. 2011, *MNRAS*, **417**, 2161
 Barnes, J., & Kasen, D. 2013, *ApJ*, **775**, 18
 Barnes, J., Kasen, D., Wu, M.-R., et al. 2016, *ApJ*, **829**, 110
 Becerra, B. L., Dichiara, S., Watson, M., et al. 2019, *ApJ*, **881**, 12
 Beniamini, P., & Nakar, E. 2019, *MNRAS*, **482**, 5430
 Berger, E. 2014, *ARA&A*, **52**, 43
 Berger, E., Fong, W., & Chornock, R. 2013, *ApJL*, **774**, L23
 Bloom, J. S., Kulkarni, S. R., & Djorgovski, S. G. 2002, *AJ*, **123**, 1111
 Bucciantini, N., Metzger, B. D., Thompson, T. A., et al. 2012, *MNRAS*, **419**, 1537
 Coughlin, M. W., Dietrich, T., Margalit, B., et al. 2018, arXiv:1812.04803
 Coulter, D. A., Foley, R. J., Kilpatrick, C. D., et al. 2017, *Sci*, **358**, 1556
 Cowperthwaite, P. S., Berger, E., Villar, V. A., et al. 2017, *ApJL*, **848**, L17
 de Ugarte Postigo, A., Thöne, C. C., Rowlinson, A., et al. 2014, *A&A*, **563**, A62
 Drout, M. R., Piro, A. L., Shappee, B. J., et al. 2017, *Sci*, **358**, 1570
 Evans, P. A., Cenko, S. B., Kennea, J. A., et al. 2017, *Sci*, **358**, 1565
 Fan, Y.-Z., & Xu, D. 2006, *MNRAS*, **372**, L19
 Fan, Y. Z., Zhang, B., & Proga, D. 2005, *ApJL*, **635**, L129
 Fernández, R., Tchekhovskoy, A., Quataert, E., et al. 2019, *MNRAS*, **482**, 3373
 Fong, W., Alexander, K. D., & Laskar, T. 2016, *GCN*, 19854, 1
 Fong, W., & Berger, E. 2013, *ApJ*, **776**, 18
 Fong, W., Berger, E., Chornock, R., et al. 2013, *ApJ*, **769**, 56
 Fong, W., Berger, E., Margutti, R., et al. 2015, *ApJ*, **815**, 102
 Freiburghaus, C., Rosswog, S., & Thielemann, F.-K. 1999, *ApJL*, **525**, L121
 Fujibayashi, S., Kiuchi, K., Nishimura, N., et al. 2018, *ApJ*, **860**, 64
 Gaia Collaboration, Brown, A. G. A., Vallenari, A., et al. 2016, *A&A*, **595**, A2
 Gaia Collaboration, Brown, A. G. A., Vallenari, A., et al. 2018, *A&A*, **616**, A1
 Gal-Yam, A., Fox, D. B., Price, P. A., et al. 2006, *Natur*, **444**, 1053
 Gao, H., Ding, X., Wu, X.-F., et al. 2015, *ApJ*, **807**, 163
 Gehrels, N., Norris, J. P., Barthelmy, S. D., et al. 2006, *Natur*, **444**, 1044
 Gehrels, N., Ramirez-Ruiz, E., & Fox, D. 2009, *ARA&A*, **47**, 567
 Ghirlanda, G., Salafia, O. S., Paragi, Z., et al. 2019, *Sci*, **363**, 968
 Gibson, S. L., Wynn, G. A., Gompertz, B. P., et al. 2017, *MNRAS*, **470**, 4925
 Gill, R., & Granot, J. 2018, *MNRAS*, **478**, 4128
 Goldstein, A., Veres, P., Burns, E., et al. 2017, *ApJL*, **848**, L14
 Gompertz, B. P., Levan, A. J., Tanvir, N. R., et al. 2018, *ApJ*, **860**, 62
 Gompertz, B. P., O’Brien, P. T., Wynn, G. A., et al. 2013, *MNRAS*, **431**, 1745
 Granot, J., Nakar, E., & Piran, T. 2003, *Natur*, **426**, 138
 Granot, J., & Piran, T. 2012, *MNRAS*, **421**, 570
 Grossman, D., Korobkin, O., Rosswog, S., & Piran, T. 2014, *MNRAS*, **439**, 757
 Harrison, R., & Kobayashi, S. 2013, *ApJ*, **772**, 101
 Hotokezaka, K., Kiuchi, K., Kyutoku, K., et al. 2013, *PhRvD*, **87**, 24001
 Ioka, K., Kobayashi, S., & Zhang, B. 2005, *ApJ*, **631**, 429
 Ioka, K., & Nakamura, T. 2019, *MNRAS*, **487**, 4884
 Jin, Z.-P., Covino, S., Liao, N.-H., et al. 2019, arXiv:1901.06269
 Jin, Z.-P., Hotokezaka, K., Li, X., et al. 2016, *NatCo*, **7**, 12898
 Jin, Z.-P., Li, X., Wang, H., et al. 2018, *ApJ*, **857**, 128
 Just, O., Bauswein, A., Ardevol Pulpillo, R., et al. 2015, *MNRAS*, **448**, 541
 Kagawa, Y., Yonetoku, D., Sawano, T., et al. 2019, arXiv:1904.10775
 Kann, D. A., Klose, S., Zhang, B., et al. 2011, *ApJ*, **734**, 96
 Kasen, D., Badnell, N. R., & Barnes, J. 2013, *ApJ*, **774**, 25
 Kasliwal, M. M., Korobkin, O., Lau, R. M., Wollaeger, R., & Fryer, C. L. 2017a, *ApJL*, **843**, L34
 Kasliwal, M. M., Nakar, E., Singer, L. P., et al. 2017b, *Sci*, **358**, 1559
 Kawaguchi, K., Shibata, M., & Tanaka, M. 2018, *ApJL*, **865**, L21
 Kisaka, S., & Ioka, K. 2015, *ApJL*, **804**, L16
 Kisaka, S., Ioka, K., & Sakamoto, T. 2017, *ApJ*, **846**, 142
 Kiuchi, K., Sekiguchi, Y., Shibata, M., et al. 2009, *PhRvD*, **80**, 64037
 Kobayashi, S. 2000, *ApJ*, **545**, 807
 Kobayashi, S., Ryde, F., & MacFadyen, A. 2002, *ApJ*, **577**, 302
 Kobayashi, S., & Sari, R. 2001, *ApJ*, **551**, 934
 Kulkarni, S. R. 2005, arXiv:astro-ph/0510256
 Kumar, P., & Piran, T. 2000, *ApJ*, **532**, 286
 Lamb, G. P., & Kobayashi, S. 2016, *ApJ*, **829**, 112
 Lamb, G. P., & Kobayashi, S. 2017, *MNRAS*, **472**, 4953
 Lamb, G. P., & Kobayashi, S. 2018, *MNRAS*, **478**, 733
 Lamb, G. P., & Kobayashi, S. 2019, *MNRAS*, **489**, 1820
 Lamb, G. P., Lyman, J. D., Levan, A. J., et al. 2019, *ApJL*, **870**, L15
 Lamb, G. P., Mandel, I., & Resmi, L. 2018, *MNRAS*, **481**, 2581
 Lattimer, J. M., & Schramm, D. N. 1974, *ApJL*, **192**, L145
 Levan, A. J., Lyman, J. D., Tanvir, N. R., et al. 2017, *ApJL*, **848**, L28
 Levan, A. J., Wiersema, K., Tanvir, N. R., et al. 2016, *GCN*, 19846, 1
 Li, L.-X., & Paczyński, B. 1998, *ApJL*, **507**, L59
 Lloyd-Ronning, N. 2018, *Galax*, **6**, 103
 Loveday, J., Norberg, P., Baldry, I. K., et al. 2015, *MNRAS*, **451**, 1540
 Lü, H.-J., Zhang, H.-M., Zhong, S.-Q., et al. 2017, *ApJ*, **835**, 181
 Margalit, B., & Metzger, B. D. 2017, *ApJL*, **850**, L19
 Matsumoto, T., Nakar, E., & Piran, T. 2019, *MNRAS*, **483**, 1247
 Mészáros, P., & Rees, M. J. 1997, *ApJ*, **476**, 232
 Metzger, B. D., Martínez-Pinedo, G., Darbha, S., et al. 2010, *MNRAS*, **406**, 2650
 Metzger, B. D., Piro, A. L., & Quataert, E. 2008, *MNRAS*, **390**, 781
 Mooley, K. P., Frail, D. A., Dobie, D., et al. 2018, *ApJL*, **868**, L11
 Nakamura, T., Kashiyama, K., Nakauchi, D., et al. 2014, *ApJ*, **796**, 13
 Nakar, E. 2007, *PhR*, **442**, 166
 Palmer, D. M., Barthelmy, S. D., Cummings, J. R., et al. 2016, *GCN*, 19844, 1

- Panaiteanu, A., Mészáros, P., & Rees, M. J. 1998, *ApJ*, 503, 314
- Pe'er, A. 2012, *ApJL*, 752, L8
- Perego, A., Rosswog, S., Cabezón, R. M., et al. 2014, *MNRAS*, 443, 3134
- Perley, D. A., Metzger, B. D., Granot, J., et al. 2009, *ApJ*, 696, 1871
- Pian, E., D'Avanzo, P., Benetti, S., et al. 2017, *Natur*, 551, 67
- Piro, L., Troja, E., Zhang, B., et al. 2019, *MNRAS*, 483, 1912
- Planck Collaboration, Ade, P. A. R., Aghanim, N., et al. 2016, *A&A*, 594, A13
- Pooley, D., Kumar, P., Wheeler, J. C., et al. 2018, *ApJL*, 859, L23
- Radice, D., Perego, A., Hotokezaka, K., et al. 2018, *ApJ*, 869, 130
- Resmi, L., & Zhang, B. 2016, *ApJ*, 825, 48
- Rossi, A., Stratta, G., Maiorano, E., et al. 2019, arXiv:1901.05792
- Rosswog, S. 2007, *MNRAS*, 376, L48
- Rosswog, S., Feindt, U., Korobkin, O., et al. 2017, *CQGra*, 34, 104001
- Rosswog, S., Sollerma, J., Feindt, U., et al. 2018, *A&A*, 615, A132
- Salafia, O. S., Ghirlanda, G., Ascenzi, S., et al. 2019, *A&A*, 628, A18
- Sari, R., & Piran, T. 1999, *ApJ*, 520, 641
- Savchenko, V., Ferrigno, C., Kuulkers, E., et al. 2017, *ApJL*, 848, L15
- Sbarufatti, B., Burrows, D. N., Osborne, J. P., et al. 2016, GCN, 19841, 1
- Schlafly, E. F., & Finkbeiner, D. P. 2011, *ApJ*, 737, 103
- Sekiguchi, Y., Kiuchi, K., Kyutoku, K., et al. 2016, *PhRvD*, 93, 124046
- Smartt, S. J., Chen, T.-W., Jerkstrand, A., et al. 2017, *Natur*, 551, 75
- Stanbro, M., & Meegan, C. 2016, GCN, 19843, 1
- Tanaka, M., & Hotokezaka, K. 2013, *ApJ*, 775, 113
- Tanaka, M., Kato, D., Gaigalas, G., et al. 2018, *ApJ*, 852, 109
- Tanvir, N. R., Levan, A. J., Fruchter, A. S., et al. 2013, *Natur*, 500, 547
- Tanvir, N. R., Levan, A. J., González-Fernández, C., et al. 2017, *ApJL*, 848, L27
- Troja, E., Castro-Tirado, A. J., Becerra Gonzalez, J., et al. 2019, arXiv:1905.01290
- Troja, E., Ryan, G., Piro, L., et al. 2018, *NatCo*, 9, 4089
- Troja, E., Tanvir, N., Cenko, S. B., et al. 2016, GCN, 20222, 1
- Tunnicliffe, R. L., Levan, A. J., Tanvir, N. R., et al. 2014, *MNRAS*, 437, 1495
- Utsumi, Y., Tanaka, M., Tominaga, N., et al. 2017, *PASJ*, 69, 101
- van Eerten, E. T. H., Ryan, G., Ricci, R., et al. 2018, arXiv:1808.06617
- Wanajo, S., Sekiguchi, Y., Nishimura, N., et al. 2014, *ApJL*, 789, L39
- Willingale, R., Starling, R. L. C., Beardmore, A. P., Tanvir, N. R., & O'Brien, P. T. 2013, *MNRAS*, 431, 394
- Wollaeger, R. T., Korobkin, O., Fontes, C. J., et al. 2018, *MNRAS*, 478, 3298
- Xu, D., Malesani, D., de Ugarte Postigo, A., Gafton, E., & Rivero Losada, I. 2016, GCN, 19834, 1
- Yang, B., Jin, Z.-P., Li, X., et al. 2015, *NatCo*, 6, 7323
- Yu, Y. B., Wu, X. F., Huang, Y. F., et al. 2015, *MNRAS*, 446, 3642
- Zhang, B., & Mészáros, P. 2002, *ApJ*, 566, 712
- Ziaepour, H. 2018, *MNRAS*, 478, 3233